Experimental and numerical analysis in heat flow sensors calibration

Experimental and numerical analysis in heat flow sensors calibration

Fausto Arpino[1], Gino Cortellessa[1], Marco Dell'Isola[1], Giorgio Ficco[1]

Fabio Bertiglia[2], Luigi Iacomini[2], Vito Fernicola[2]

[1] Dipartimento di Ingegneria Civile e Meccanica, Università degli Studi di Cassino e del Lazio Meridionale, via G. Di Biasio 43, Cassino, Italy

[2] Istituto Nazionale di Ricerca Metrologica (INRIM), Strada delle Cacce, 91 - 10135 Torino, Italy

Corresponding author:
Dr. G. Cortellessa
Dipartimento di Ingegneria Civile e Meccanica, Università degli Studi di Cassino e del Lazio Meridionale, Via G. Di Biasio 43, 03043 Cassino (FR), Italy
e-mail: g.cortellessa@unicas.it

keywords:
Heat Flow Sensor (HFS) calibration system, experimental thermodynamics, numerical modelling, thermal conductivity, thermal analysis, uncertainty analysis.

Abstract

The 2010/31/CE directive has highlighted the necessity to improve the energy efficiency in buildings, since they are responsible for 40% of energy consumption and 36% of CO_2 emissions in the EU. In situ measurements of envelope components are needed for estimating the thermal transmittance of existing buildings in order to perform the energy certification. The instruments devoted to this aim are, the Heat Flux Meters (HFMs), unfortunately not always are provided with metrological traceability, and appropriate reference standards are not available. The calibration systems currently adopted present different limits related to low performances at low and constant heat fluxes, non-uniformity of the heat flux in the measurement section and impossibility to control the heat flux at different temperatures.

In this paper the authors discuss the metrological behaviour of an existing HFM reference standard. A numerical model is employed to analyse the calibration system in different operating conditions (low and moderate heat fluxes), to improve it and to design a new prototype presenting high performances also in presence of the Heat Flux Sensor (HFS) under calibration. In particular, the numerical tool is applied to investigate the heat flux uniformity and the metrological performances in a specific sub-region of the measuring section where the HFS under calibration is applied. A detailed experimental analysis is also conducted with the objective to validate the adopted numerical tool. Moreover, a metrological characterization of the system affords a combined standard uncertainty of better than 6% at low heat flows.

1. Introduction

Improvements in the energy efficiency of buildings are called upon by European directives, such as the 2002/91/CE, which sets the maximum values of energy needs and thermal transmittance of building envelope components. [1]. In situ measurements of envelope components are needed for: (i) estimating the thermal transmittance of existing buildings in order to perform the energy certification and (ii) validating the energy performance design of new buildings. When the design data about existing buildings are not available, it can be necessary to perform invasive tests to detect stratigraphy and materials properties. Alternatively, the thermal transmittance can be measured in situ, according to ISO 9869:2005 [2], by means of an Heat Flux Meter (HFM). Since measurement conditions are usually not stationary while the thermal conductance has to be obtained in steady-state conditions, long measurement runs are required to perform accurate in situ estimations. An HFM is basically made of a thin plate of known thermal conductivity, and by an integrated system for the measurement of the temperature difference across the plate itself. Time-consuming measurements and a proper data post-processing procedure are required to overtake not stationary conditions and to allow for the thermal conductance calculation. The design, calibration and application method of HFM have been standardized through the ASTM C1130:2017 [3], C177:2013 [4], ISO 8302:1991 [5], ASTM C 518:2017 [6], ISO 8301:1991 [7].

Influence quantities which affect the calibration accuracy are, among others: (i) the operating temperature, (ii) the thickness of the reference specimen, (iii) the overall thermal conductance of the layer between the hot and cold plates, (iv) the contact resistance at the various interfaces, and (v) the uniformity of the heat flux [8].

Therefore, the design of a suitable calibration apparatus for HFM must allow for an independent control of the thermal flux crossing the HFM and the average temperature in the measurement section.

Even though in the last few years, several studies were conducted to investigate the metrological performance of HFMs [9-11] and the associated calibration procedures [12-14], the devices employed in building applications are often uncalibrated and, consequently, the measurement traceability cannot be guaranteed.

This happens because the measurement chain (made of a flow sensor, two or more temperature sensors and a data acquisition system) is quite complex and suitable standards are not always available at the national metrology institutes (NMIs) level to provide the first step in the traceability chain.

Looking at the scientific literature, some authors designed Guarded Hot Plate (GHP) devices but mainly for the purpose of measurement the thermal conductivity. In particular, Dubois [15] presented a GHP apparatus designed for thermal conductivity measurement of high thickness crop-based specimens. High thickness samples, up to 40 cm, with an accuracy of 2% were analysed.

Reid [16] designed a GHP for high temperature applications. This apparatus was designed to measure thermal conductivity of soils at different moisture contents and for temperature ranging from -20°C to 200°C. An error around 2% was found for the thermal conductivity measurement.

Tleoubaev [17] developed a combined GHP and heat flow meter method for absolute thermal conductivity tests of moderate thermal conductivity materials (up to 10 W/mK). This combination of the two traditional steady-state methods provided significantly increased accuracy of the absolute thermal conductivity measurements of important materials such as ceramics, glasses, plastics, rocks, polymers, composites and fireproof materials [18].

Reddy [19] designed a double-sided square guarded hot plate (SGHP) apparatus specifically for testing low to moderate thermal conductivity materials having thermal conductivities in the range of 0.02-3.0 $Wm^{-1}K^{-1}$. Le Quang [20] studied the size effect on the effective through-thickness conductivity of heterogeneous plates showing that the size effect of the effective through-thickness conductivity is more significant than the one of the effective in-plane conductivity. Liu [21] performed numerical simulations with turbulence methods to study the effect of unsteady thermal boundary conditions on the temporal behaviour of heat transfer coefficient on a flat plate. Some authors of the present paper, designed a standard system for HFM calibration [22]. The results were affected by a high heat flux distortion and showed that in order to minimize the uncertainty of the generated heat flux, a very fine temperature control on the side thermal guard was needed.

A critical aspect which need a careful investigation in an HFM calibration is the dependences of the calibration curve from the temperature gradient across it and from the average temperature in the measuring section. The design of an adequate calibration apparatus should be able to vary, independently, such parameters.

In this work the authors perform a numerical investigation of an HFM reference standard operating at low and moderate heat fluxes between 10 W/m^2 and 100 W/m^2. The prototype is designed and realized in collaboration between the University of Cassino and Lazio Meridionale (UNICLAM) and the Istituto Nazionale di Ricerca Metrologica (INRIM). In this system, the heat flux over the measurement section is determined by measuring the temperature difference across a certified reference material with known thermal conductivity. Preliminary heat flux measurements are performed assembling the calibration system in absence of the HFS, but heat flux distortion could appear when the calibration system is used in real conditions. Therefore, a numerical model is selected and applied to investigate the heat flux uniformity and temperature fields necessary to improve the prototype performances in presence of the HFS. The temperature and heat flux measurements, obtained by the existing calibration system for average heat fluxes of about 10 W/m^2, 50 W/m^2 and 100 W/m^2, are compared to the numerical results, in order to validate the numerical model. An uncertainty analysis is performed and a combined standard uncertainty equal to 5.7% at low heat flows is found. Finally, the validated numerical tool is applied to an extensive parameter analysis of the HFM prototype metrological performance. In this way, the best

metrological performances of heat flux uniformity are determined in presence of the HFS under calibration and the design of an improved prototype of the HFM standard is realized.

2. Calibration system

The proposed HFM standard prototype is visible in Figure 1, while a sketch of the prototype asymmetric section is available in Figure 2, where a description of different components of the calibration system is reported. The prototype is cylindrical and the bold dash-dot line represents its symmetry axis. Heat flux is generated from an electrical heater driven by a Proportional-Integral-Derivative (PID) controller, and passes through an aluminium plate (hot plate) and three Pyrex glass plates (Pyrex samples 73, 60 and 59) with a known thickness and certified thermal conductivity, to homogenize the flow. The system is closed on the top from a water heat exchanger in brass, connected at a thermostatic bath, to keeps fixed the temperature (cold plate). The measurement section, where the HFM under calibration is positioned, is placed in E-F, between the aluminium plate and brass layer. Above the brass heat exchanger, a layer of Armaflex insulating material is adopted. In order to minimize thermal dispersion to the surrounding environment, the central part is separated in radial direction, by an air gap of 2 mm, from a passive guard consisting of several concentric borosilicate ring, wound in an insulating mat. The system keeps the temperature difference across the air gap and across a Teflon layer (placed between the main and the guard heater) below 0.01°C, using two guard heaters driven by a PID controller. In particular, a lower guard heater is placed on the bottom of the system and a guard ring is placed around the main heater (see Figure 2). The temperature difference between the main heaters and the lower guard is measured employing two Platinum Resistance Thermometers PRTs Pt-100, while the temperature difference between main and side guard (ring heater) is measured by 8 type-J differential thermocouples evenly distributed on the annular interface between the heaters and connected in series. In such a way the heat power (W) supplied by the main heater is directed to the measurement section E-F, where the HFS under calibration must be positioned. The measurement section is a circular surface with a diameter of 0.3 m and, to minimize the distortion of heat flux lines, it is supposed to use complementary plate of similar material of the HFS under calibration to cover the whole measurement surface, avoiding the presence of air gaps.
The heat flux across the HFS under calibration is determined by the Equation (1) reported in the next section: the Pyrex thermal conductivity $\lambda_t\ (W/m^{-1}K^{-1})$ is known by the certificate material, the temperature difference $\Delta T_{C-A}\ (K)$ (between points A and C) across the certificated material is measured by two calibrated Pt100 and the thickness of the measurement section is known $s_t\ (m)$ [14, 23]. The heat flux dispersions in radial direction are evaluated by monitoring the temperature of the ring in the points B and D. Experimental and numerical investigations are performed for three different values of the main heater power in order to generate an estimated heat flux of 10 W/m^2, 50 W/m^2 and 100 W/m^2, from the main heater towards the measuring section.

3. Uncertainty analysis

A measurement uncertainty analysis of the experiments, based on the ISO/IEC guideline on uncertainty estimation [24, 25], is performed and presented in the following. As described in Section 2, the experimental apparatus allows for heat flux meters to be calibrated by measuring the temperature drop across the reference glass layer.
When the temperature drop across the CRM glass layer is measured, the heat flux is estimated by the following equation:

$$\emptyset = \frac{\lambda_t \cdot \Delta T_{C-A}}{s_t} \tag{1}$$

where:

- λ_t is the Pyrex® glass thermal conductivity, in W m^{-1} K^{-1};
- ΔT_{C-A} is the temperature drop across the Pyrex® glass (temperature difference between points *C* and *A* in Figure 2), K;
- s_t is the thickness of a set of three glass layers (each of thickness s_i), m.

The combined standard uncertainty of the measured heat flux is obtained by the following equation:

$$u_\emptyset = \sqrt{\left(\frac{\Delta T_{C-A}}{s_t}\right)^2 u_{\lambda_t}^2 + \left(\frac{\lambda_t}{s_t}\right)^2 u_{\Delta T_{C-A}}^2 + \left(\frac{\lambda_t \cdot \Delta T_{C-A}}{s_t^2}\right)^2 u_{s_t}^2} \tag{2}$$

where:

- u_{λ_t} is the standard uncertainty of the Pyrex® thermal conductivity (from the reference material certificate), W m^{-1} K^{-1};
- $u_{\Delta T_{C-A}}$ is the standard uncertainty associated with the temperature drop across the glass layers, K;
- u_{s_t} is the standard uncertainty of the thickness of the set of three Pyrex layers, m.
-

The Pyrex® glass thermal conductivity is determined by employing the equation for conduction in solid:

$$\lambda_t = \frac{s_t}{R_t} = \frac{\sum_{i=1}^{3} s_i}{\sum_{i=1}^{3} \left(\frac{s_i}{\lambda_i}\right)} \quad (3)$$

where $R_t = R_1 + R_2 + R_3$ ($m^2 K W^{-1}$) is the total thermal resistance to the heat flux given by three layers in series, each of thermal resistance $R_i = s_i/\lambda_i$. In this case, considering the correlation among the R_i estimations, u_{R_t} is calculated as follows:

$$u_{R_t} = \sqrt{u_{R_1}^2 + u_{R_1}^2 + u_{R_1}^2 + 2r\left(u_{R_1}u_{R_2} + u_{R_1}u_{R_3} + u_{R_2}u_{R_3}\right)} \quad (4)$$

The uncertainty associated with the conductivity u_{λ_t} is estimated by the following equation:

$$u_{\lambda_t} = \sqrt{\left(\frac{1}{R_t}\right)^2 u_{st}^2 + \left(\frac{s_t}{R_t^2}\right)^2 u_{R_t}^2} \quad (5)$$

The standard uncertainty of the temperature drops across the Pyrex® glass $u_{\Delta T_{C-A}}$ is:

$$u_{\Delta T_{C-A}} = \sqrt{2(u_t^2 + u_c^2) + u_{un}^2} \quad (6)$$

where:

- u_t is the calibration uncertainty of the temperature sensors, K;
- u_c is the uncertainty contribution due to the thermal contact, K;
- u_{un} is the uncertainty contribution due to the contact surface uniformity, K.

The standard uncertainty associated with the thickness of a set of three glass layers, u_{s_t}, is estimated through the corresponding uncertainties of each *i-th* pyrex layer u_{s_i}, in turns estimated with the following equation:

$$u_{s_i} = \sqrt{u_l^2 + \frac{RES^2}{12} + \left(\frac{\sigma_i}{\sqrt{N_i}}\right)^2} \quad (7)$$

$$u_{s_t} = \sqrt{u_{s_1}^2 + u_{s_2}^2 + u_{s_3}^2 + 2r\left(u_{s_1}u_{s_2} + u_{s_1}u_{s_3} + u_{s_2}u_{s_3}\right)} \quad (8)$$

where:

- u_l is the calibration standard uncertainty of the gauge instrument, m;
- RES is the resolution of the gauge instrument, m;
- $\sigma/\sqrt{N}$ is a type-A uncertainty [26, 27] associated with the standard deviation σ of N measurements, mm.
- r is the correlation coefficient assumed equal to 0.5, since measurements of single layer thickness have been performed with the same instrument.

In

Table 1 the estimated expanded uncertainties for the developed calibration apparatus are summarized.

4. Mathematical model

Numerical investigations allowed a better understanding of heat flux uniformity, temperature and velocity fields necessary to improve the new prototype performances. The experimental apparatus is reproduced by a two-dimensional axial symmetric computational domain, that is available in Figure 3 together with the boundary conditions employed and a detail of the computational grid, composed by 80045 triangular elements and chosen on the basis of a mesh sensitivity analysis. Temperature distribution inside the proposed HFM standard prototype has been numerically reproduced through modern Computational Fluid Dynamic (CFD) technique Simulations employing the finite element based commercial software Comsol Multiphysics®. The computational domain and the boundary conditions employed are available in Figure 3. The temperature fields are obtained by solving the well-known energy conservation equations [22-24], not

reported here for brevity. In order to accurately reproduce experiments, three generation terms are applied in correspondence of the main and guard heaters indicated in yellow in Figure 1.
An appropriate set of boundary conditions (BCs) are imposed and indicated within the computational domain (

Figure a). In particular, a constant and uniform temperature (T_{water}) is imposed between the insulating foam panels and the brass plates to reproduce the thermal effect of the thermostatic bath. Additionally, a convective heat flux is evaluated and applied on the right vertical wall and the lower surface of the computational domain, while an adiabatic boundary condition is applied to the upper horizontal surface.
The control of the heat flux is numerically performed by integrating Comsol Multiphysics® with a numerical code implemented in Matlab. In particular, the following calculation steps are followed:

i) impose a heat power on the main heater;
ii) ii) perform first simulation with zero heat power imposed in correspondence of the two guard heaters;
iii) calculate the temperature difference across the mean heater and the lower guard heater in axial direction and between the main heater and the side guard heater in the radial direction;
iv) if temperature differences are larger than 0.01°C then increase/decrease heat power of the two guards and repeat simulation until convergence.

5. Results and validation

In order to improve the existing calibration system, also considering the presence of the HFM, the selected numerical model has been firstly validated by the experimental data available in the case of heat flux of 10 W/m^2, 50 W/m^2 and 100 W/m^2. Based on available measurements, the main input parameters for numerical simulation are reported in Table 2. The temperature contour, as obtained for heat flux equal to 100 W/m^2, 50 W/m^2 and 10 W/m^2 and thermostatic bath temperature respectively equal to 32.80 °C, 31.55 °C and 29.76 °C are shown in Figure 4a, Figure 4c and Figure 4d.
In all the investigated cases, the maximum temperature is reached in proximity of the main heater while the surrounding environment presents the lowest temperature. Figure 4b, Figure 4d and Figure 4e, represents the heat flux contour along the radial direction, in the 5 W/m^2 to -5 W/m^2 span. Small radial heat flux dispersions are visible in the measurement section (lower than 1 W/m^2). The green zones clearly indicate that in all the cases the heat flux radial dispersions are fairly limited thanks to the effective operation of the lower and radial thermal guards.
Comparisons between experiments and numerical results for the investigated heat fluxes are available in Table 3 for heat fluxes of 100 W/m^2, 50 W/m^2 and 10 W/m^2, respectively. The tests were carried out with a surrounding environment temperature equal to 23 °C.
In order to obtain a heat flux of 100 W/m^2 from the main heater towards the measurement section, a heat-source power of 7.07 W is numerically imposed in the heater domain and later measured by the electric power delivered to the main heater. Similarly, source power terms in the simulation and measured electric powers are 3.53 W for a heat flux of 50 W/m^2, and 0.71 W for a heat flux of 10 W/m^2 (Table 3).
In the case of a nominal heat of flux 100 W/m^2, the average heat flux across the three Pyrex® layers, estimated by Equation (1) is equal to 99.67 W/m^2. Similarly, when a heat flux of 50 W/m^2 leaves the main heater towards the direction of the measurement section, the heat flux estimated by Equation (1) is equal to 49.60 W/m^2. Finally, in the case of a heat flux of 10 W/m^2 the estimate is equal to 9.49 W/m^2 (Table 3).
Comparing the heat flux values as measured by the Equation (1) with the numerical results, a difference of 0.23 % is observed for a heat flux of 100 W/m^2 (test number 1). When a heat flux of 50 W/m^2 is applied, the heat flux difference obtained is equal to 0.26 (test number 2). Finally adopting a heat flux of 10 W/m^2, the heat flux difference obtained is equal to 0.94 % (test number 3). The measurement uncertainty associated with the measured heat flux ranges between 5.7%, when the heat flux is equal to 10 W/m^2, and 2.8%, when the heat flux is 100 W/m^2. As shown, experiments and numerical results are compatible and the proposed numerical model is validated.
In Table 3, the results are also shown in terms of temperature in the selected points A, B, C and D (see Figure 2) and temperature difference between points A and C (to estimate the axial temperature variation among the glass plates).
In the case of 100 W/m^2, the deviation in the temperature between points C and A is equal to 0.08°C, in the case of 50 W/m^2, the experimental-to-numerical temperature deviation is equal to about 0.03°C, while in the case of 10 W/m^2, it amounts to 0.09°C.

6. Design of a new prototype of the HFM standard by numerical investigations

The validated numerical tool is adopted in order to improve the heat flux uniformity in presence of the HFS. The current version of the prototype presents a uniform heat flux in the measurement section. In fact, the temperature differences between the points A and B and between points C and D (see Table 3) are very limited (max ΔT_{A-B}=0.2°C for test n.2). However, when a further layer representing the HFS under calibration is added over the measurement section (see Figure 2), the performances of the calibration system are reduced, because the HFS present a lower thermal conduction (λ=0.76 W/mK) in respect to the aluminium (λ=120 W/mK). Therefore, a radial heat flux dispersion appears and the heat flux on the HFS to be calibrated is lower compared to that generated by the main heater.
Different simulations were carried out by, varying the geometry, in order to optimize the heat flux uniformity in the measurement section, in the presence of HFS. In the simulations, the same boundary conditions reported in Figure 3a and

the same input parameters listed in Table 2 were adopted, with the exception of the environment temperature set to a constant value of 25°C.
In Figure 5 the sketch of an axisymmetric section showing the final configuration is reported. Compered to the existing configuration the new design presents different changes.
In particular: i) the thickness of the expanded rubber has been doubled, ii) the guard heater has been extended, completely covering the aluminium layer, iii) the axial air gap has been extended to the polystyrene, reducing the radial dispersion from the main heater to the guard ring, iv) an additional layer composed by the HFS (radius of 40 mm), its mask and polystyrene on the side thermal guard have been added. In Figure 6, a comparison between the radial heat flux contours obtained activating and disabling the regulation system is illustrated. In these simulations, the heat flux imposed on the mean heater is equal to 100 W/m^2 and the thermostatic bath temperature is of 20°C. The heat flux in the computational domain is limited between -5 W/m^2 and 5 W/m^2 to amplify the effects of the radial dispersions. From the analysis of this figure, it is possible to observe that the regulation system is necessary in order to obtain a uniform 1D axial heat flux. Therefore, when the regulation system is activated, the green zones in Figure 6a clearly indicate that the radial dispersion are limited. In Figure 7 and in Table 4, the deviations between numerical heat fluxes in the measurement section and the heat fluxes imposed at the main heater (100 W/m^2, 50 W/m^2 and 10 W/m^2) are reported as a function of the liquid bath temperature. It is evident that for lower liquid bath temperatures, lower heat flux deviations are obtained. However, the bath temperature present limit values below which the regulation system is not able to regulate. This happen because, when the calibration system works at a lower average temperature than the environment, a radial heat flux enters the system from outside. On the contrary, increasing the thermostatic bath temperature, the heat flux deviations increase because the radial heat flux dispersion became greater and the regulation system is not able to control.
The quantitative results of Table 4 highlights that in correspondence of a thermostatic bath temperature equal to 24°C, the heat flux deviations are lower than 0.4 % for all the investigated heat fluxes ranging between 100 W/m^2 and 10 W/m^2. Finally, the effects on the heat flux uniformity in the measurement section E-F of the calibration system, as a function of the HFS radius (in the range 0 m$\leq$r$\leq$0.040 m), are reported in Figure 8. An excellent uniformity, for the three heat fluxes imposed at the main heater (100 W/m^2, 50 W/m^2 and 10 W/m^2) is found.

7. Conclusions

In the present paper, the authors perform a numerical investigation of an HFM reference standard developed in collaboration between UNICLAM and INRIM, operating at low and moderate heat fluxes between 10 W/m^2 and 100 W/m^2. The temperature distribution and the heat flux uniformity are numerically investigated by solving the well-known energy conservation equations, employing the finite element based commercial software Comsol Multiphysics®. In order to validate the numerical tool, an experimental campaign is carried out encompassing the generated heat fluxes of 10 W/m^2, 50 W/m^2 and 100 W/m^2. A detailed uncertainty analysis of the generated heat flux is conducted. The combined standard uncertainty affecting the measured heat flux according to the relative method ranges between 5.7 %, at the lowest heat flux, and 2.8 % when the heat flux is near 100 W/m^2. Preliminary heat flux measurements are performed assembling the calibration system in absence of the HFS, but heat flux distortion appear when the calibration system is used in real conditions.
Therefore, the selected numerical model is applied to investigate the heat flux uniformity and temperature fields necessary to improve the prototype performances in presence of the HFS. The obtained quantitative results highlight that in correspondence of a thermostatic bath temperature equal to 24°C, the deviations between numerical heat fluxes in the measurement section and the heat fluxes imposed at the main heater are lower than 0.4% for all the investigated heat fluxes. In addition, an excellent uniformity of the heat flux is found in the measurement section E-F of the calibration system. In this way, the best metrological performances of heat flux uniformity are determined in presence of the HFS under calibration and the design of an improved prototype presenting higher performances is realized.

8. References

1. European Commission. 2018. https://ec.europa.eu/energy/en/topics/energy-efficiency/buildings.
2. ISO 9869-1:2014, Thermal insulation - Building elements - In-situ measurement of thermal resistance and thermal transmittance - Part 1: Heat flow meter method. ISO; 2014.
3. ASTM C1130: Standard Practice for Calibration of Thin Heat Flux Transducers. ASTM INTERNATIONAL; 2017.
4. ASTM C177-13: Standard Test Method for Steady-State Heat Flux Measurements and Thermal Transmission Properties by Means of the Guarded-Hot-Plate Apparatus. ASTM International; 2013.
5. ISO 8302: Thermal insulation - Determination of steady-state thermal resistance and related properties - Guarded hot plate apparatus. ISO; 1991.
6. ASTM C518-17: Standard Test Method for Steady-State Thermal Transmission Properties by Means of the Heat Flow Meter Apparatus. ASTM International; 2017.
7. ISO 8301: Thermal insulation - Determination of steady-state thermal resistance and related properties - Heat flow meter apparatus. ISO; 1991.
8. Guattari C, Evangelisti L, Gori P, Asdrubali F. Influence of internal heat sources on thermal resistance evaluation through the heat flow meter method. Energy and Buildings. 2017;135:187-200. doi:10.1016/j.enbuild.2016.11.045.
9. Van der Graaf F. Heat flux sensors. In: W.Gopel, editor. Sensors. New York1989. p. 295-322.

10. Flanders SN. Heat flux trasducers measure in-situ building thermal performance. Journal of Thermal Insulation and Building Environments. 1994;18:28-52.
11. Hauser RL. Construction and performance of in situ heat flux trasducers. In: Bales, editor. Building Applications of Heat Flux Trasducers - ASTM STP 885. 1985. p. 172-83.
12. Murthy V, Tsai B, Saunders R, editors. Facility for calibrating heat flux sensors at NIST: an overview. ASME Heat Transfer Division; 1997; New York.
13. Lackey J, Normandin N, Marchand R, Kumaran K. Calibration of Heat Flow Meter Apparatus. J Thermal Insul and Bldg Envs. 1994;18:128-44.
14. Bomberg M, Solvason KR. Comments on Calibration and Design of Heat Flow Meter. Thermal Insulation, Materials and Systems fo Energy Conservation in the '80s - ASTM STP 789. 1983:277-92.
15. Dubois S, Lebeau F. Design, Construction and Validation of a Guarded Hot Plate Apparatus for Thermal Conductivity Measurement of High Thickness Crop-Based Specimens. Materials and structures. 2013;48(1-2):407-21.
16. Reid D. Guarded hot plate apparatus design and construction for thermal conductivity measurements. Toronto, Ontario, Canada: Ryerson University; 2005.
17. Tleoubaev A, Brzezinski A. Combined Guarded-Hot-Plate and Heat Flow Meter Method for Absolute Thermal Conductivity Tests Excluding Thermal Contact Resistance. Thermal Conductivity 27/Thermal Expansion 15; Knoxville,Tennessee,USA2003.
18. Arpino F, Cortellessa G, Dell'Isola M, Ficco G, Marchesi R, Tarini C, editors. Influence of Installation Conditions on Heating Bodies Thermal Output: Preliminary Experimental Results. Energy Procedia; 2016.
19. Reddy KS, Jayachandran S. Investigations on design and construction of a square guarded hot plate (SGHP) apparatus for thermal conductivity measurement of insulation materials. Int J Therm Sci. 2017;120:136-47. doi:10.1016/j.ijthermalsci.2017.06.001.
20. Le Quang H, Pham DC, Bonnet G. Size effect in through-thickness conductivity of heterogeneous plates. Int J Therm Sci. 2014;79:40-50. doi:10.1016/j.ijthermalsci.2013.12.013.
21. Liu CL, Gao C, von Wolfersdorf J, Zhai YN. Numerical study on the temporal variations and physics of heat transfer coefficient on a flat plate with unsteady thermal boundary conditions. Int J Therm Sci. 2017;113:20-37. doi:10.1016/j.ijthermalsci.2016.11.013.
22. Arpino F, Dell'Isola M, Ficco G, Iacomini L, Fernicola V. Design of a calibration system for heat flux meters. International Journal of Thermophysics. 2011;32(11-12):2727-34. doi:10.1007/s10765-011-1054-3.
23. Bomberg M, Solvason KR. Discussion of Heat Flow Meter Apparatus and Transfer Standards Used for Error Analysis. Guarded Hot Plate and Heat Flow Meter Methodology - ASTM STP 879. 1985. p. 140-53.
24. UNI CEI 70098-3: Incertezza di misura - Parte 3: Guida all'espressione dell'incertezza di misura. UNI; 2016.
25. BIPM. Evaluation of measurement data - The role of measurement uncertainty in conformity assessment2012.
26. Coleman HW, Steele WG. Experimentation and Uncertainty Analysis for Engineers. 2 ed. USA: 1999.
27. Betta G, Dell'Isola M, Frattolillo A. Experimental design techniques for optimising measurement chain calibration. Measurement: Journal of the International Measurement Confederation. 2001;30(2):115-27. doi:10.1016/s0263-2241(00)00060-9.

Table 1. Expanded uncertainty of the calibration apparatus.

∅ Nominal heat flux, Wm^{-2}	*$U_{∅}$, Expanded uncertainty %*
10	5.7
50	3.2
100	2.8

Table 2. Main input parameters used in the numerical investigations.

Parameter	Value
Ambient temperature, T_a	23.0 °C
Ambient pressure, p_a	101325 Pa
Water temperature, T_{water}	29.75 °C - 32.80 °C
Main heater power, E_p	7.07 W - 3.53 W - 0.71 W
Pyrex conductivity, $\lambda_{pyrex}(T)$	$1.1036+1.659\times10^{-3}T-3.982\times10^{-6}T^2+6.764\times10^{-9}T^3$ W/m/K
Pyrex density, ρ_{pyrex}	2230 kg/m^3
Pyrex specific heat, $c_{p,pyrex}$	837 J/kg/K
Aluminum conductivity, $\lambda_{aluminum}$	120 W/m/K
Aluminum density, $\rho_{aluminum}$	2702 kg/m^3
Aluminum specific heat, $c_{p,aluminum}$	896 J/kg/K
Rubber pad conductivity, λ_{rubber}	0.073 W/m/K
Rubber pad density, ρ_{rubber}	1000 kg/m^3
Rubber pad specific heat, $c_{p,rubber}$	1000 J/kg/K
Teflon conductivity, λ_{teflon}	0.23 W/m/K
Teflon density, ρ_{teflon}	2140 kg/m^3
Teflon specific heat, $c_{p,teflon}$	1000 J/kg/K
Polystyrene, conductivity, $\lambda_{polystyrene}$	0.054 W/m/K
Polystyrene, density, $\rho_{polystyrene}$	15 kg/m^3
Polystyrene specific heat, $c_{p,polystyrene}$	1220 J/kg/K
Armaflex, conductivity, $\lambda_{polystyrene}$	0.038 W/m/K
Armaflex, density, $\rho_{polystyrene}$	70 kg/m^3
Armaflex specific heat, $c_{p,polystyrene}$	1000 J/kg/K

Table 3. Comparison between the experiments and numerical results obtained in correspondence of three different heat flux, generated by the main heater, equal to 10, 50 and 100 W/m^2.

Test number	**1**	**2**	**3**
Heat flux at the main heater (W/m^2)	100	50	10
Thermostatic bath temperature (°C)	32.80	31.55	29.76
Heat power at the main heater (W)	7.07	3.53	0.71
Experimental temperature of point A (°C)	33.95	32.34	30.07
Numerical temperature of point A (°C)	33.98	32.35	30.07
Experimental temperature of point B (°C)	33.90	32.14	29.81
Numerical temperature of point B (°C)	33.97	32.35	30.07
Experimental temperature of point C (°C)	43.79	37.26	31.02
Numerical temperature of point C (°C)	43.73	37.24	31.03
Experimental temperature of point D (°C)	43.76	37.23	31.02
Numerical temperature of point D (°C)	43.75	37.25	31.03
Experim. ΔT between point C and point A (°C)	9.84	4.92	0.95
Numerical ΔT between point C and point A (°C)	9.76	4.89	0.96
Heat power at the radial guard heater (W)	16.17	8.44	2.72
Heat power at the lower guard heater (W)	7.39	4.19	2.51
Experimental heat flux (evaluated by Equation 1) (W/m^2)	99.67±2.79	49.60±1.59	9.49±0.54
Numerical average heat flux on the pyrex (W/m^2)	98.75	49.25	9.56
Numerical heat flux in section E-F (W/m^2)	98.52	49.11	9.47

Table 4. Heat flux deviation as a function of the thermostatic bath temperature, evaluated in correspondence of the heat flux equal to 100 W/m^2, 50 W/m^2 and 10 W/m^2.

	Heat flux deviation (%)		
Thermostatic bath temperature (°C)	Φ= 100 W/m^2	Φ= 50 W/m^2	Φ= 10 W/m^2
30	0.952	1.452	5.161
28	0.789	1.058	2.731
26	0.544	0.676	0.893
24	0.349	0.208	0.223

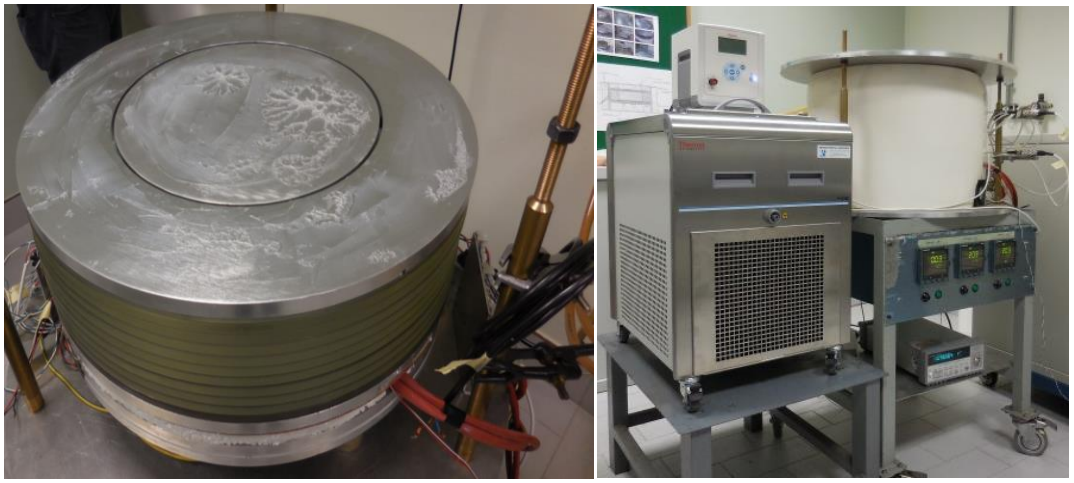

Figure 1. Prototype of the HFS standard assembled system.

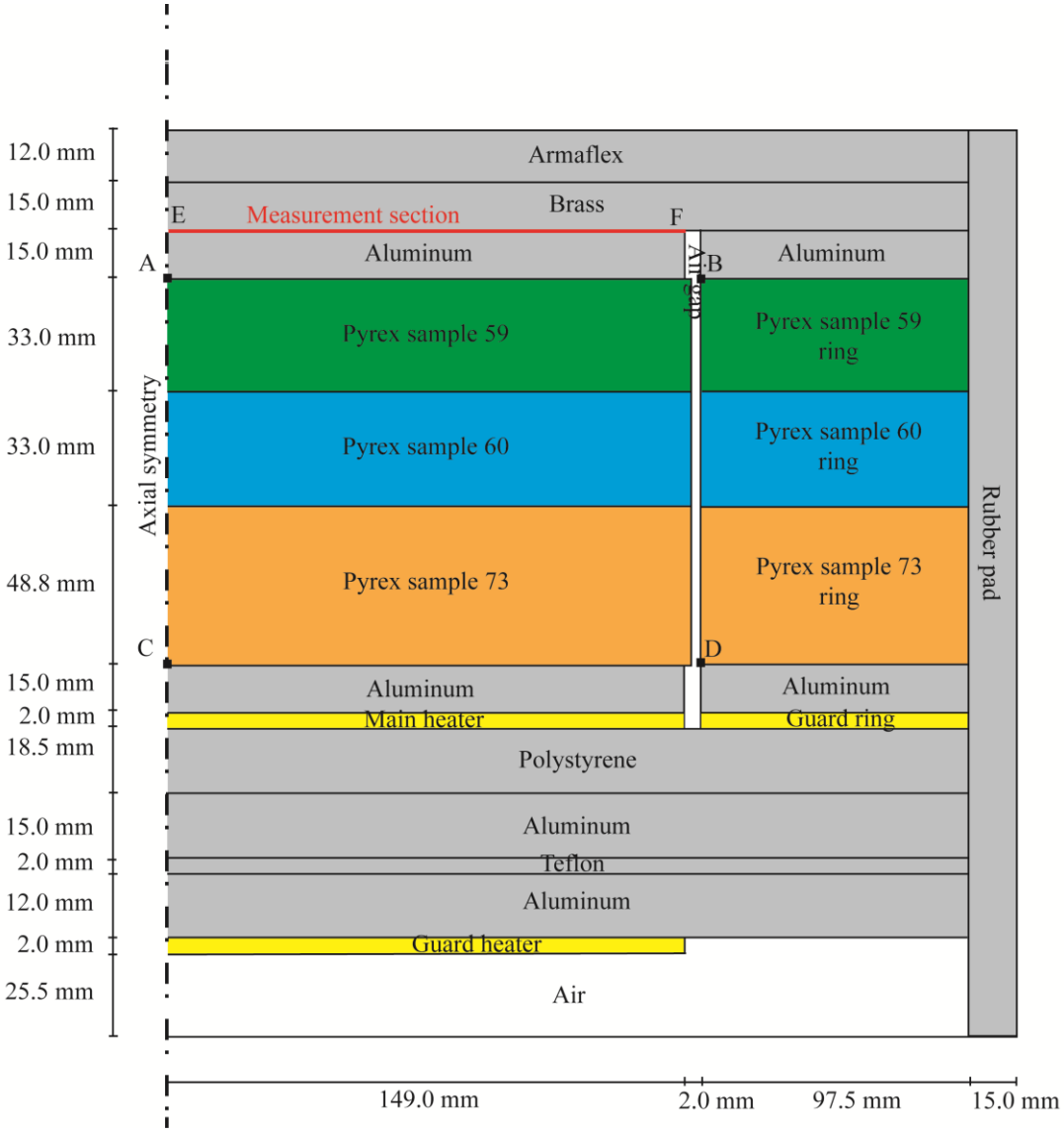

Figure 2. Existing HFS standard: sketch of an axisymmetric section showing different components.

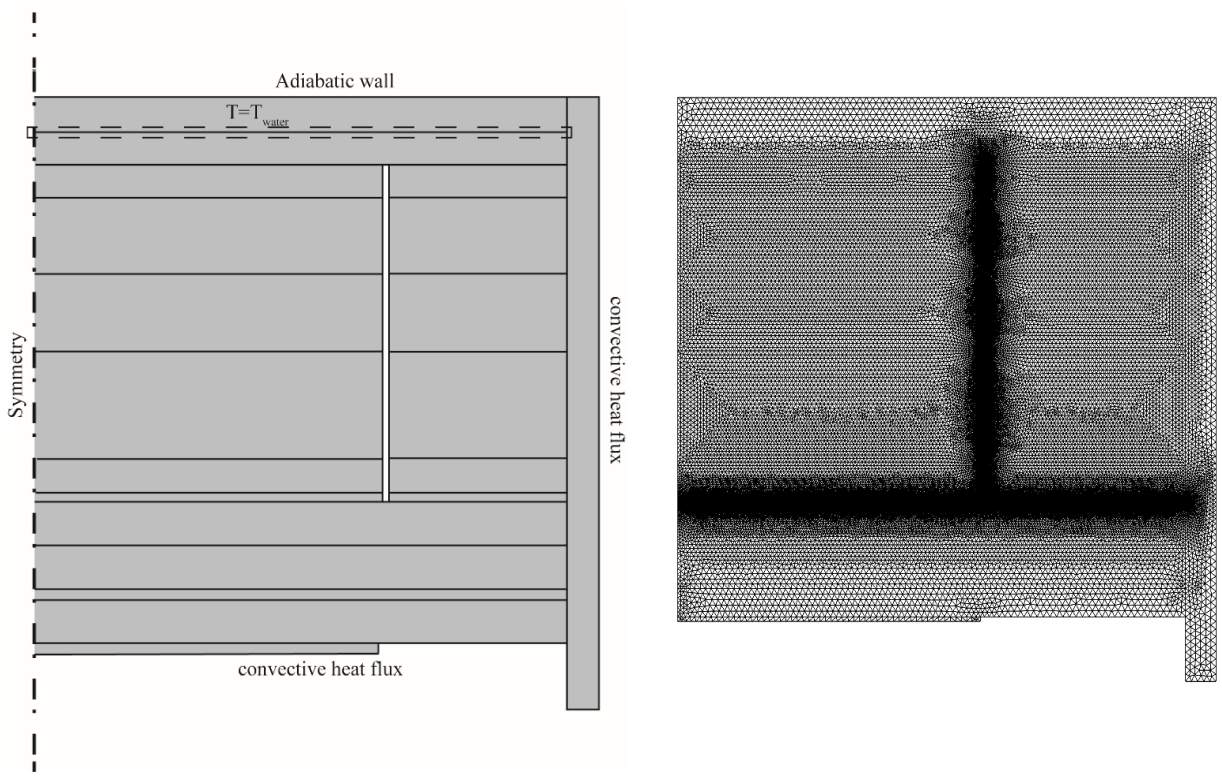

(a) (b)

Figure 3. Numerical simulation of the HFM standard prototype: computational domain and boundary condition employed (left) and a detail of the computational grid composed by 80045 triangular elements (right).

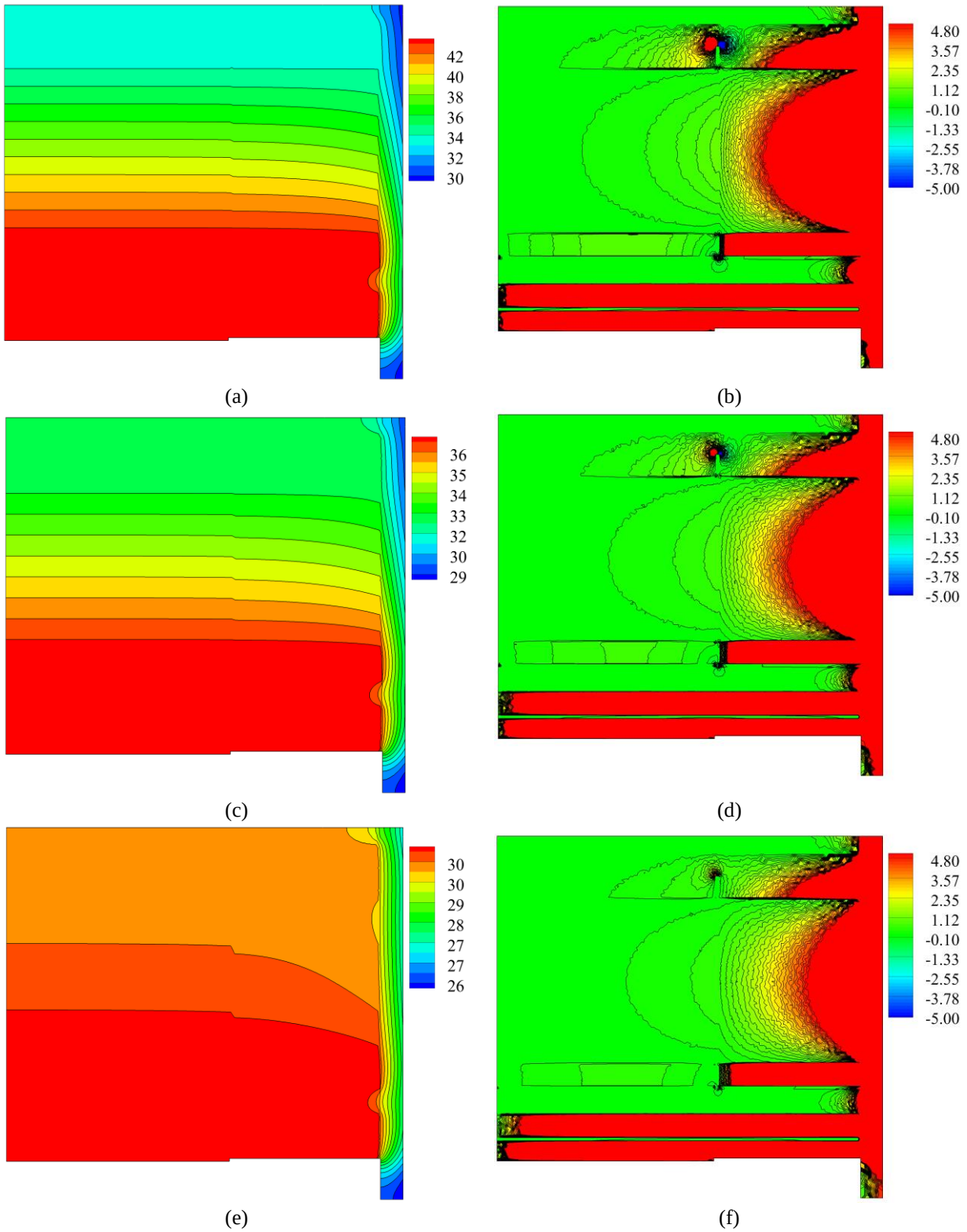

Figure 4. Temperature contour and radial heat flux limited between -5 W/m^2 and 5 W/m^2 obtained for generated heat flux on the mean heater equal to 100 W/m^2 (a, b), 50 W/m^2 (c, d) and 10 W/m^2 (e, f).

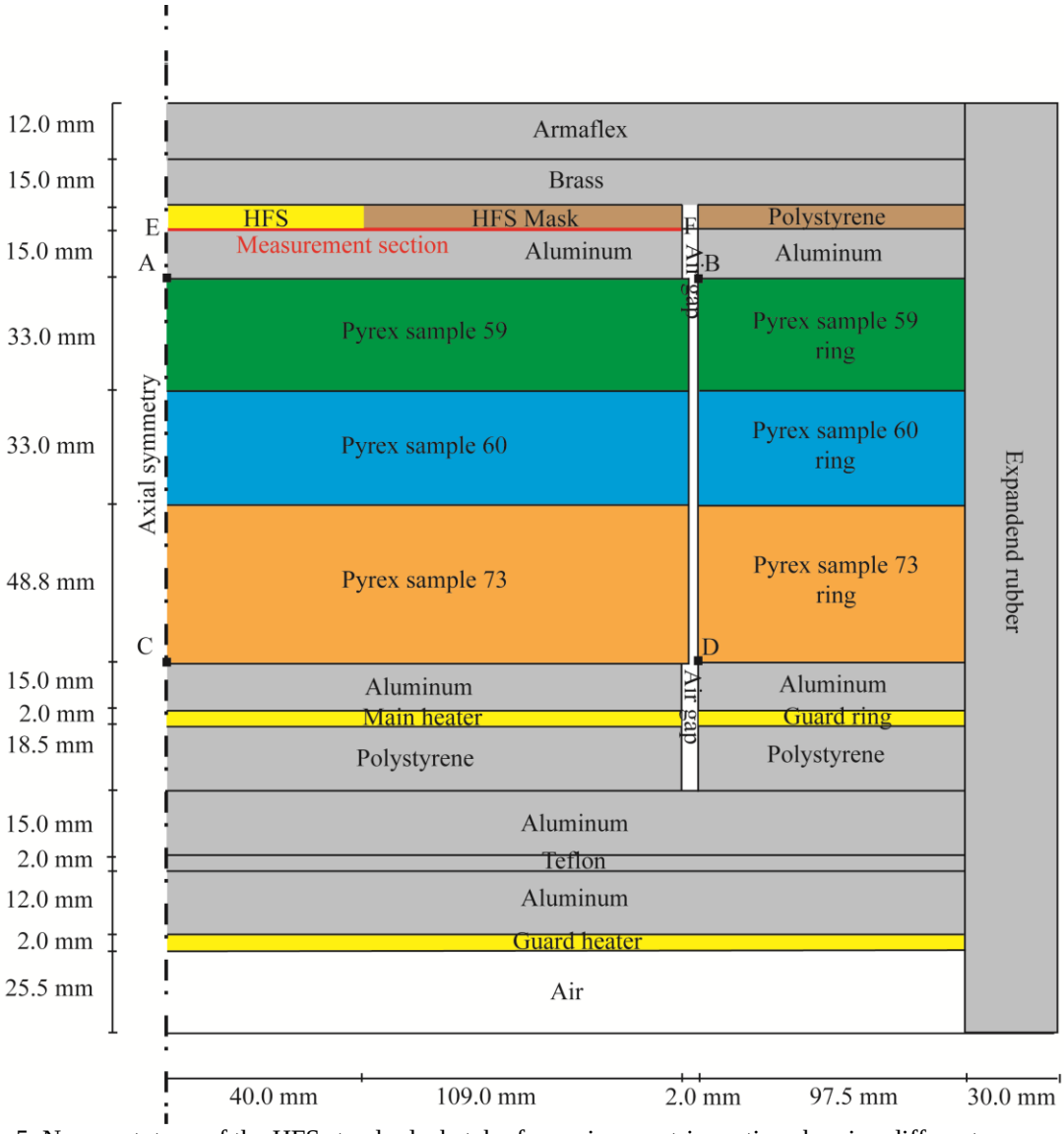

Figure 5. New prototype of the HFS standard: sketch of an axisymmetric section showing different components.

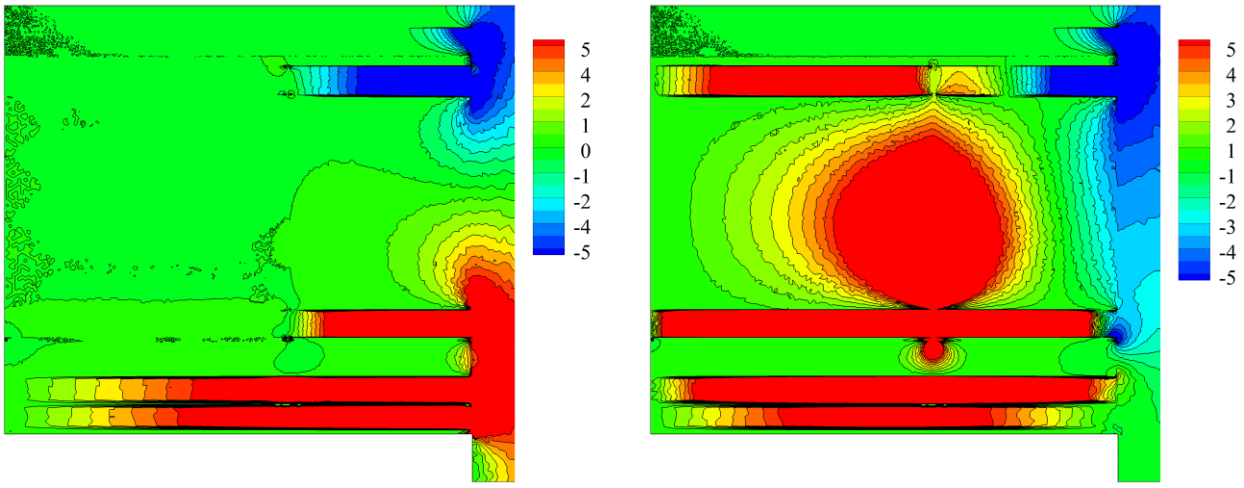

(a) (b)

Figure 6. Radial heat flux limited between -5 W/m^2 and 5 W/m^2 obtained for generated heat flux on the mean heater equal to 100 W/m^2 and thermostatic bath temperature of 20°C: system regulation activated (a), system regulation disabled (b).

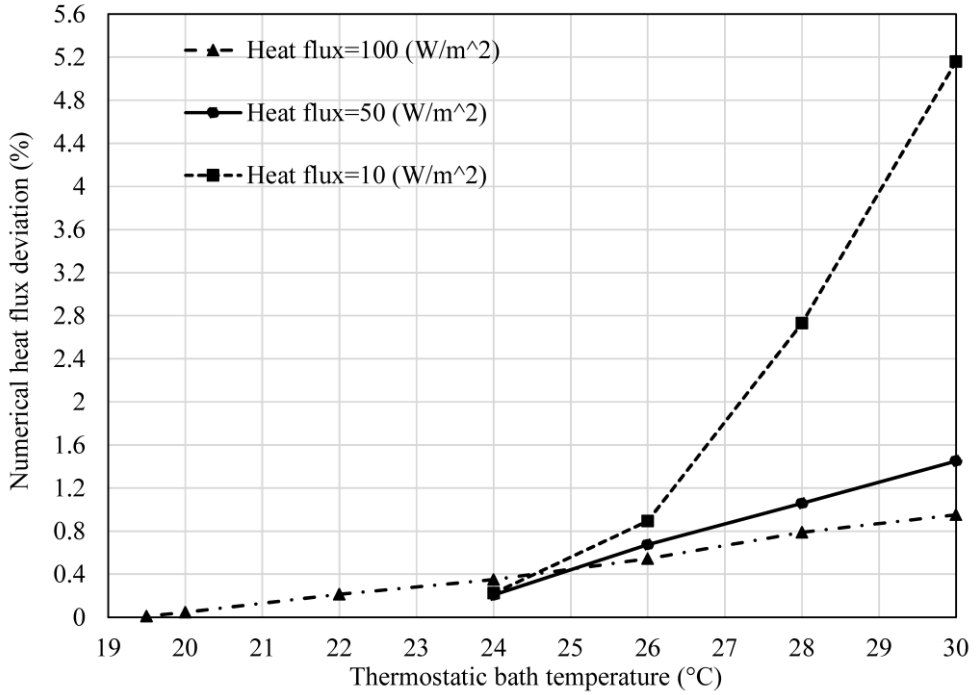

Figure 7. Numerical heat flux deviations as a function of the thermostatic bath temperature obtained for generated heat flux on the mean heater equal to 100 W/m^2, 50 W/m^2 and 10 W/m^2.

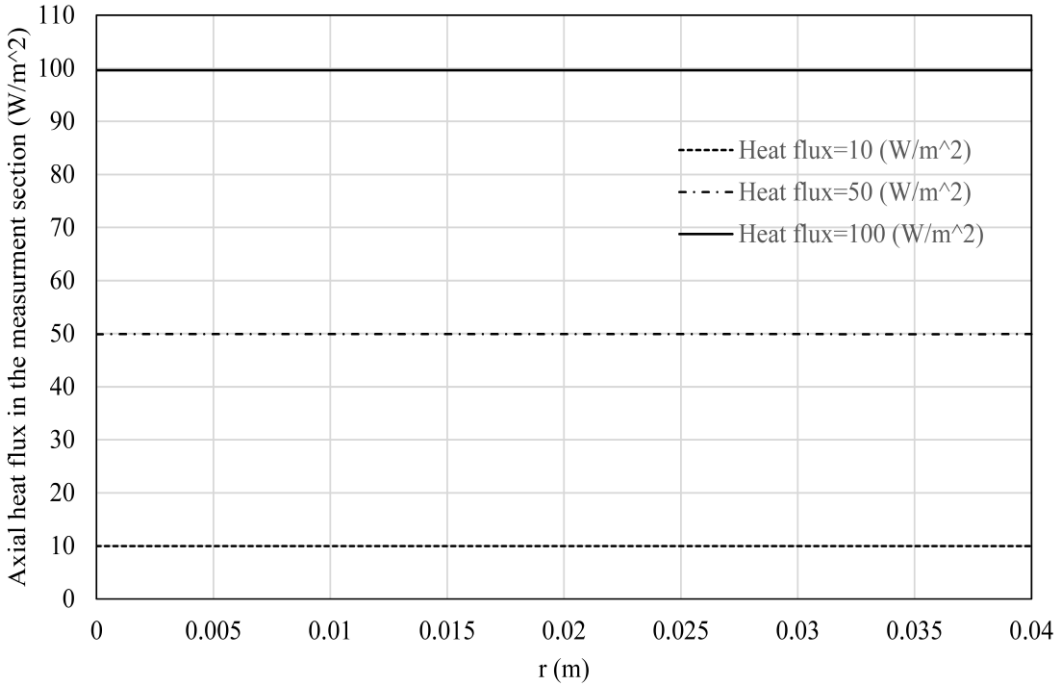

Figure 8. Heat flux axial profiles obtained in the measurement section (E-F) as a function of the radius covering portion of the ring necessary for the HFS calibration, for a thermostatic bath temperature equal to 24°C.